Influences of the buoyancy of partially molten rock on 3-D plume patterns and melt productivity above retreating slabs

Guizhi Zhu [a,*], Taras V. Gerya [a,b], Satoru Honda [c], Paul J. Tackley [a], David A. Yuen [d]

[a] *Department of Earth Sciences, Swiss Federal Institute of Technology (ETH Zurich), CH-8092 Zurich, Switzerland*
[b] *Geology Department, Moscow State University, 119899 Moscow, Russia*
[c] *Earthquake Research Institute, University of Tokyo, Tokyo 113-0032, Japan*
[d] *Department of Geology and Geophysics and Minnesota Supercomputing Institute, Minneapolis, MN 55455-0219, USA*

ABSTRACT

Using 3-D petrological-thermo-mechanical subduction models, we investigate how the buoyancy of partially molten rock affects the development of thermal–chemical plumes and melt productivity in the mantle wedge. As a first order approximation we limit the positive buoyancy of partially molten rock (compared to non-molten rock), which can be decreased due to rapid melt extraction and removal to the surface. Our simulations show that a large to moderate density contrast ($\Delta\rho$) of >200 kg/m^3 between non-molten (η_{n-m}) and partially molten rock (η_{p-m}). (i.e. low to moderate degree of melt removal from rock) promotes the development of three distinct patterns of plumes (finger-like, ridge-like and wave-like). In contrast, a low density contrast ($\Delta\rho$) of 0–50 kg/m^3 (i.e. high to complete melt removal) suppresses pronounced plumes and is associated with low-amplitude (50–100 km wide and 10–15 km high) domal structures developing atop the slab due to the chemical buoyancy of subducted hydrated non-molten rock types (oceanic crust, sediments, serpentinites). Variation in partially molten rock viscosity (η_{p-m}) also notably affects plume patterns and lateral dimensions: wave-like plumes are most pronounced at higher ($\eta_{p-m} = 10^{19}$ Pa s) viscosity, which also favors the development of larger plumes compared to models with lower ($\eta_{p-m} = 10^{18}$ Pa s) viscosity. Integrated melt productivity above the slab is notably higher for cases with pronounced hydrated thermal–chemical plumes developed in the mantle wedge. Indeed, all models are characterized by periodic (5–10 Myr long episodes of enhanced productivity), spatially clustered (30–50 km distance between productivity maxima) melt production, which may explain the periodicity and clustering of volcanic activity observed in magmatic arcs such as in North-East Japan and New Zealand.

© 2011 Elsevier B.V. All rights reserved.

1. Introduction

Subduction zones are the dominant physical and chemical systems of Earth's interior (Stern, 2002). It is widely accepted that ambient mantle rock melting with the help of dehydration of subducting slabs is an important interactive process between fluid and solid mantle in the mantle wedge (e.g. Mysen and Boettcher, 1975; Peacock, 1990; Davies and Stevenson, 1992; Iwamori, 1998; van Keken et al., 2002; Arcay et al., 2005; Hebert et al., 2009). Since the fluid is released from the subducting slab, it alters physical–chemical properties of the overlying mantle rock (e.g. Karato and Wu, 1993; Poli and Schmidt, 1995; Schmidt and Poli,

1998; Connolly and Petrini, 2002; Asimow and Langmuir, 2003; Gerya and Yuen, 2003b; Grove et al., 2006; Plank et al., 2009), for instance, by lowering their melting temperature, viscosity and density. Multiple numerical studies using coupled thermal–chemical models have already been performed on subduction processes in different geodynamic settings exploring various physical parameters, such as slab age (Gorczyk et al., 2006; Nikolaeva et al., 2008; Hebert et al., 2009), convergence velocity (Gorczyk et al., 2006; Cagnioncle et al., 2007; Faccenda et al., 2008), slab dip angle (Hebert et al., 2009; Cagnioncle et al., 2007; Grove et al., 2009), and fluid propagation velocity (Gerya and Yuen, 2003b; Nikolaeva et al., 2008; Honda et al., 2010; Gorczyk et al., 2007). It was also demonstrated that the shape of seismic velocity anomalies in the mantle wedge and the volcano distribution can be reproduced by the thermal–chemical models (Gerya et al., 2006, 2004c; Gorczyk et al., 2006,2007; Hebert et al., 2009; Cagnioncle et al., 2007).

Presently, the inherently three-dimensional (3-D) subduction process and its resultant geophysical, petrological and magmatic

* Corresponding author. Tel.: +41 44 633 2907; fax: +41 44 633 1065.
E-mail addresses: guizhi.zhu@erdw.ethz.ch (G. Zhu), taras.gerya@erdw.ethz.ch (T.V. Gerya), Honda@eri.u-tokyo.ac.jp (S. Honda), paul.tackley@erdw.ethz.ch (P.J. Tackley), daveyuen@gmail.com (D.A. Yuen).

phenomena (Tamura et al., 2002; Honda and Yoshida, 2005; Zhao et al., 2002; Zhao, 2009) have been mostly studied by using two-dimensional (2-D) thermal–chemical subduction models including ad hoc fluid migration and melting processes (e.g. Gerya and Yuen, 2003b; Arcay et al., 2005; Gorczyk et al., 2006; Cagnioncle et al., 2007; Nikolaeva et al., 2008; Hebert et al., 2009; Grove et al., 2009). These 2-D studies allowed the delineation of important regularities in the spatial distribution and dynamics of hydration and melting above slabs (e.g. Davies and Stevenson, 1992; Cagnioncle et al., 2007; Hebert et al., 2009; Grove et al., 2009) but lateral variability of these processes along magmatic arcs (e.g. Tamura et al., 2002; Honda and Yoshida, 2005) remained unknown.

Three-dimensional thermal–chemical subduction modeling efforts with high enough spatial resolution are still rare. Using 3-D petrological-thermomechanical models of subduction, Zhu et al. (2009) explored the influence of the effective viscosity of partially molten rock on the development of strongly chemically buoyant plumes above retreating slabs. Their results show that three types of 3-D Rayleigh-Taylor instabilities (cold plumes) may develop in the mantle wedge: finger-like plumes that form a sheet-like structure parallel to the trench; ridge-like structures perpendicular to the trench; and flattened wave-like instabilities propagating upwards along the upper surface of the slab and forming zig-zag patterns subparallel to the trench. It also demonstrated that a lower viscosity of partially molten rock above slabs ($\eta_{p-m} = 10^{18}$–10^{19} Pa s), one to two orders less than the viscosity in the surrounding mantle (Fig. 2d in Zhu et al., 2009), favors plume development at short wavelengths, which is consistent with the conditions for small-scale thermal convection in the mantle wedge as derived from 3-D modeling (Honda et al., 2002; Honda and Yoshida, 2005). Recently, Honda et al. (2010) developed a simplified 3-D model of convection in the mantle wedge driven by both thermal and chemical buoyancy above the kinematically prescribed subducting slab. They found that the chemically altered region tends to stay in the corner of the mantle wedge and suppress 3-D thermal instability in the mantle wedge.

Comparison of numerical results from the 3-D subduction models of Zhu et al. (2009) and Honda et al. (2010) suggests that 3-D thermal–chemical convection patterns (and hence melt productivity distribution) in the mantle wedge can be strongly variable and depend on both the magnitude and spatial distribution of chemical buoyancy above slabs. In the relatively simple constant viscosity model of Honda et al. (2010) with kinematically prescribed slab velocity only transient mushroom-like and sheet-like plumes were developing during subduction and the stability of other thermal–chemical buoyant structures such as ridge-like plumes, wave-like plumes, zig-zag plume patterns etc. in our self-consistent free subduction model (Zhu et al., 2009) were not revealed. Also, in their model, Honda et al. (2010) used the assumption that the density of hydrated mantle remains constant and does not depend on P-T conditions. However, notable density variations with temperature and pressure are expected due to influences of phase transformations and melting processes (e.g. Hebert et al., 2009; Zhu et al., 2009). On the other hand, the more complex subduction model of Zhu et al. (2009) used a thermodynamic database for computing the density of partially molten hydrated rock based on the assumption of negligible melt removal from the rock. This resulted in relatively large density contrasts (up to $\Delta \rho > 300$ kg/m^3) between non-molten (η_{n-m}) and partially molten rock (η_{p-m}). However, the positive buoyancy of partially molten rock should be significantly influenced by melt extraction and rapid removal to the surface (e.g. Nikolaeva et al., 2008; Hebert et al., 2009; Connolly et al., 2009). These processes are clearly indicated by the magmatic activity and crustal growth occurring in volcanic arcs fueled by the intense fluid release from subducting slabs. The efficiency and rates of melt extraction and removal can be variable in nature and depend
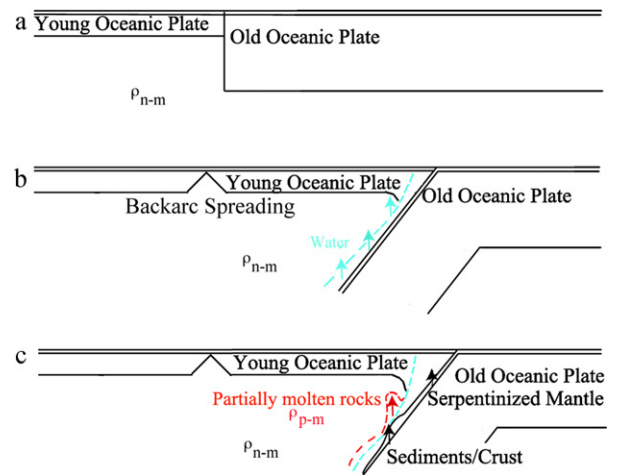

Fig. 1. Conceptual model of spontaneously retreating intraoceanic subduction. (a) Initial subduction setup with old oceanic plate and young oceanic plate. All the rock is non-molten with a density of ρ_{n-m}. (b) Water release from the subducting slab, which is shown by blue arrows, during spontaneously retreating subduction. The water front is shown by the blue dashed line. A spreading center forms underneath the overriding plate. All the rock is non-molten with a density of ρ_{n-m} before melting. (c) Serpentinized mantle forming inside the overriding plate, while sediments and oceanic crust are subducted with the slab. Once mantle rock gets hydrated at high temperature, it partially melts. The melt front is shown by red dashed line. The water front is shown by blue dashed line. Non-molten rock still keeps the reference density of ρ_{n-m}, and partially molten rock has a density of ρ_{p-m}. Arrows show the tendency to move upwards because of buoyancy: red arrows are for partially molten rock while black arrows are for subducted serpentines, sediments and oceanic crust. (For interpretation of the references to color in this sentence, the reader is referred to the web version of the article.)

on several factors including rock grain size, melt composition, melt channeling dynamics etc. (e.g. Hawkesworth et al., 1997; Connolly et al., 2009). A high degree of melt extraction and fast removal to the surface can be generally expected for primitive low-viscosity basaltic melts generated from the mantle (e.g. Connolly et al., 2009). In contrast, a lower degree of extraction should be characteristic for more viscous silicic melts that can form (Castro and Gerya, 2008) in the ascending thermal–chemical plumes composed of subducted tectonic mélanges (Gerya and Yuen, 2003b; Zhu et al., 2009).

In our self-consistent free subduction model, water release from the slab favors serpentinized mantle and partially molten plumes. Serpentinites, sediments and oceanic crust were subducted along the subducting slab. The density contrast ($\Delta \rho$) between non-molten (η_{n-m}) and partially molten rock (η_{p-m}) would influence plume patterns and melt productivity atop the slabs, as shown in Fig. 1. The aim of this paper is to investigate how the effective buoyancy of partially molten rock affects the stability of various thermal–chemical plumes morphologies (Zhu et al., 2009) and melt productivity in the mantle wedge. In our 3-D intra-oceanic subduction model we impose an upper cutoff value ($\Delta \rho$) for the density contrast between non-molten (ρ_{n-m}) and partially molten rock (ρ_{p-m}). As a first order approximation, this cutoff value reflects melt removal from rock: the lower is the cutoff value, the smaller is the maximal melt fraction that can be present in partially molten rock.

2. Thermal–chemical convection models

2.1. Model set-up and boundary condition

We use the 3-D numerical I3ELVIS code based on a conservative finite difference method with a marker-in-cell technique and multigrid solver (Gerya and Yuen, 2003a, 2007; Gerya, 2010). The initial thermal–chemical model setup (including initial con-

ditions, boundary condition and fluid/melt transport mechanism) and numerical approach are the same as was used in our previous paper (Zhu et al., 2009) and are also detailed in the Appendix.

2.2. Effective density of partially molten rock

In our models, the in situ rock density is interpolated to every marker at each time step from look-up density tables (in P-T space) pre-computed with the Perple_X program for each of the four rock compositions involved (see Appendix). Additional density correction is performed for hydrated rock based on a constant effective water density (1050 kg/m^3) and the actual water content computed for every marker at each time step from the water migration model (see Appendix). According to results of 2-D numerical experiments, melt removal from partially molten rock has a strong influence on the development of thermal–chemical plumes atop the subducting slab (Nikolaeva et al., 2008; Hebert et al., 2009). In order to simulate the influence of a variable degree of melt removal on plume growth in 3-D, we prescribe an upper cutoff value $\Delta\rho$ for the density contrast between reference non-molten (ρ_{n-m}) and partially molten rock (ρ_{p-m}) (in our numerical experiments, $\Delta\rho$ ranges from 0 to 300 kg/m^3). A higher value of $\Delta\rho$ is interpreted as a larger melt fraction remaining in the partially molten rock. With these limitations, then the effective density of partially molten rock $\rho_{p-m(eff)}$ can be described as follows:

$$\rho_{p-m(eff)} = \begin{cases} \rho_{n-m} - \Delta\rho; & \text{if}(\rho_{n-m} - \rho_{p-m}) \geq \Delta\rho \\ \rho_{p-m}; & \text{if}(\rho_{n-m} - \rho_{p-m}) < \Delta\rho \end{cases}$$

where ρ_{p-m} and ρ_{n-m} are the density of respectively partially molten and reference non-molten rock calculated with the Perple_X program at the same local P-T conditions and rock composition (see Appendix). In these calculations, the density of the reference non-molten rock (ρ_{n-m}) was computed with the melt-absent thermodynamic database. It is worth noting that our model limits the density difference between reference non-molten (ρ_{n-m}) and partially molten rock (ρ_{p-m}) and not between pure solid and pure melt phases. By this we assume that melt fraction in partially molten rock may be reduced by processes of rapid melt extraction and removal to the surface (e.g. Nikolaeva et al., 2008; Hebert et al., 2009). These processes are, however, not modeled explicitly due to technical limitations in 3-D. In contrast to Honda et al. (2010), no density limitation is applied to hydrated rock that is not partially molten.

In order to isolate influences of the density contrast between non-molten and partially molten rock on 3-D plume morphologies, the viscosity of partially molten rock is taken to be constant and does not depend on the imposed limitation for the density contrast. Indeed, different viscosities of partially molten rock ($\eta_{p-m} = 10^{18}$–10^{19} Pa s) are tested.

3. Numerical results

3.1. Influence of partially molten rock buoyancy on plume stability

In order to investigate the influence of partially molten rock buoyancy on plume development atop the slab, we have performed two sets of runs with a lower effective viscosity of partial molten rock ($\eta_{p-m} = 10^{18}$–10^{19} Pa s), with each set of runs having a different density contrast cutoff $\Delta\rho$ for partially molten rock (see Table 1): $\Delta\rho = 300$ kg/m^3 (taking ~500 kg/m^3 difference in density between pure solid and pure melt phases, this $\Delta\rho$ implies that up to ~60 vol.% melt can be present in partially molten rock), 200 kg/m^3 (up to ~40% melt), 100 kg/m^3 (up to ~20% melt), 50 kg/m^3 (up

to ~10% melt), 30 kg/m^3 (up to ~6% melt), 10 kg/m^3 (up to 2% melt), and 0 kg/m^3 (complete melt removal). Below, we concentrate on analyzing reference models with moderate density contrast ($\Delta\rho = 200$–300 kg/m^3) and zero density contrast ($\Delta\rho = 0$ kg/m^3).

In Fig. 2(a–c), we show plume development in model 2 of Table 1, in which the effective viscosity of partially molten rock is $\eta_{p-m} = 10^{18}$ Pa s and $\Delta\rho = 200$ kg/m^3. In the early stages (1–6 Myr after the beginning of the numerical calculation), finger-like plumes develop atop the flat slab in a trench-parallel roll-like structure close to the trench (Fig. 2a), but it is much easier to form a zig-zag pattern compared to the case without a limit on the density contrast (Zhu et al., 2009), and the distribution obviously varies along the trench. During the time period 6–11 Myr, the finger-like plumes decay and the front of the thermal–chemical instabilities with small random finger-like plumes becomes sheet-like and in a zig-zag pattern followed by several trench-normal ridge-like instabilities (Fig. 2b). These changes in plume dynamics are the result of both changing slab dip and evolution of the non-steady thermal structure of the model (e.g. cooling of the overriding plate) after subduction initiation. Afterwards, pronounced plumes gradually disappear with the bending of the subducting slab and the cooling of the overriding plate (Fig. 2c). Compared to the case without a limit on the density contrast (Zhu et al., 2009), there are no wave-like plumes in the late stages (>25 Myr) of these numerical experiments.

In Fig. 2(d–f) we show the case with zero density contrast between reference non-molten (ρ_{n-m}) and partially molten rock (ρ_{p-m}) ($\Delta\rho = 0$ kg/m^3, model 7 in Table 1), which may be expected for complete instantaneous melt removal. In the early period from the beginning of the calculation, random trench-parallel and trench-normal instabilities tend to develop along the slab (Fig. 2d), then low-amplitude (50–100 km wide and 10–15 km high) dome-like instabilities (Fig. 2e) form, and afterwards there is no temperature anomaly atop the slab (Fig. 2f). The dome-like instabilities are caused by the lowered density of hydrated non-molten rock present atop the slab (sediments, oceanic crust, hydrated/serpentinized mantle that typically have 50–300 kg/m^3 density contrast with dry mantle, see Appendix) and appear in all experiments with prescribed low density contrast cutoff ($\Delta\rho = 50$ kg/m^3) between reference non-molten (ρ_{n-m}) and partially molten rock (ρ_{p-m}).

In Fig. 3(a–f), the dynamics of plumes is shown by the 1350 K temperature isosurface in the models with increased effective viscosity ($\eta_{p-m} = 10^{19}$ Pa s) of partially molten rock and $\Delta\rho = 200$ kg/m^3 (model 2′ in Table 1). In this case, in the early period (1–4 Myr from the beginning of the numerical calculation), finger-like plumes show up atop a trench-parallel sheet-like structure, and flattened instabilities seem to crawl upwards along the slab in a trench-normal way (Fig. 3a). With the upward propagation of the plumes, trench-normal ridges tend to develop and small finger-like plume clusters develop at the top of the ridges (cf. Fig. 3b and c). With the steepening of the subducting slab and the cooling of the overriding plate, small finger-like plumes disappear, and trench-normal ridges clearly develop atop the slab until they gradually decay (cf., Fig. 3d–f). Afterwards there is no pronounced temperature anomaly above the slab. However, at a later stage (8–28 Myr) wave-like structures appear in such models (Table 1), and the wave plume breaks up into several pieces at greater depth with the entrainment of upper plate materials toward the trench, the cooling and thickening of the overriding lithosphere.

Now we discuss plume development in the model with higher density contrast cutoff of 300 kg/m^3 (model 1′ in Table 1) between reference non-molten (ρ_{n-m}) and partially molten rock (ρ_{p-m}). Here we observe a mature plume development (Fig. 4(a–f)). In the early stages (1–6 Myr from the beginning of the calculation), finger-like plumes develop in trench-parallel structures

Table 1
Description of numerical experiments.

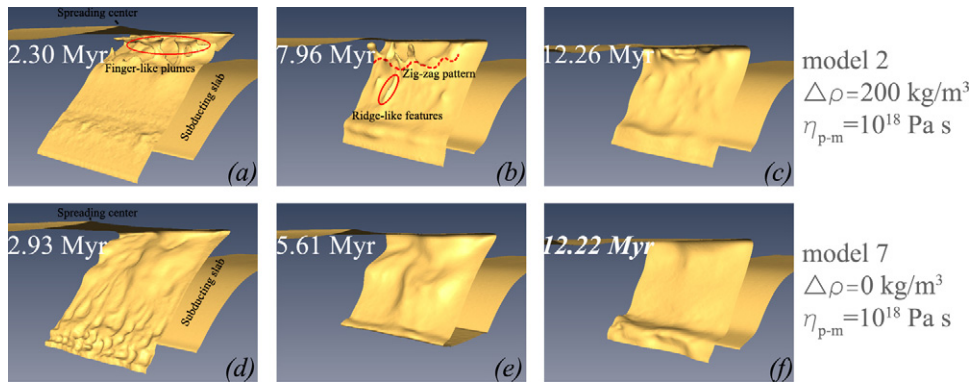| Model (run time, Myr)	Effective viscosity of partially molten rock (Pa s)	Density difference cutoff due to partially melting (kg/m³)	Development of thermal/chemical plumes		
			Plumes description	Time of appearance (Myr)	Spacing along the trench (km)
			Finger-like plumes developing atop a trench-parallel roll-like structure	1–6	20–50
			Ridge-like trench-normal plumes	6–9	30–50
			Randomly distributed unpronounced temperature anomaly	9–32	50–70
2 (27)	1e + 18	200	Finger-like plumes developing atop a trench-parallel sheet-like structure	1–4	30–50
			Randomly distributed small finger/sheet/ridge-like plume cluster along the slab	5–12	30–50
			Randomly distributed with unpronounced temperature anomaly	12–32	50–100
3 (27)	1e + 18	100	Finger-like plumes developing atop a trench-parallel sheet-like structure	1–3	30–70
			Randomly distributed small finger-like plumes	3–17	20–100
			Randomly distributed unpronounced temperature anomaly	17–27	>100
4 (27)	1e + 18	50	Roll/sheet-like instabilities along the slab	1–2	>100
			Dome-like instabilities atop the slab	3–9	>100
			Randomly distributed with unpronounced temperature anomaly	9–27	>70
5 (27)	1e + 18	30	Finger/sheet-like instabilities developing along the slab	1–1.5	50–70
			Dome-like instabilities atop the slab	1.5–6	>70
			Without any pronounced temperature anomaly	6–27	
6 (28)	1e + 18	10	Roll/sheet-like instabilities developing along the slab	1–1.5	*
			Dome-like instabilities atop the slab	1.5–9	
			Without any pronounced temperature anomaly	9–28	
7 (27)	1e + 18	0	Roll/sheet-like instabilities developing along the slab	1–1.5	*
			Dome-like instabilities atop the slab	1.5–8	
			Without any pronounced temperature anomaly	8–27	
1′ (29)	1e + 19	300	Finger-like plumes developing atop a trench-parallel roll-like structure	1–6	20–50
			Ridge-like trench-normal plumes with strong finger/sheet-like plumes on the top	6–13	50–70
			Wave-like plumes forming zig-zag structures	13–26	70–100
			Ridge-like trench-normal plumes with finger-like plumes on the top	26–29	50–100
2′ (30)	1e + 19	200	Finger-like plumes developing atop a trench-parallel sheet-like structure	1–4	50–100
			Ridge-like trench-normal plumes with small finger plume cluster along the slab	4–11	50–100
			Ridge-like trench-normal plumes	11–16	50–100
			Without any pronounced temperature anomaly	16–30	
3′ (29)	1e + 19	100	Sheet-like instabilities along the slab	1–4	*
			Small-finger like plumes in zig-zag pattern	4–15	50–100
			Without any pronounced temperature anomaly	15–29	*
4′ (32)	1e + 19	50	Randomly distributed small domes	1–4	80–100
			Without any pronounced temperature anomaly	4–33	*
5′ (33)	1e + 19	30	Randomly distributed big domes	1–5	*
			Without any pronounced temperature anomaly	5–33	*
6′ (29)	1e + 19	10	Randomly distributed big domes	1–6	*
			Without any pronounced temperature anomaly	5–29	*
7′ (34)	1e + 19	0	Randomly distributed big domes	1–6	*
			Without any pronounced temperature anomaly	5–34	*

* means the wavelength of the plume is infinite.

Fig. 2. Development of thermal–chemical structures (plumes, domes) shown by the 1350 K isosurface (models 2 and 7 in Table 1) with $\triangle\rho = 200$ kg/m^3 (a–c) and $\triangle\rho = 0$ kg/m^3 (d–f). In these models, the effective viscosity of partially molten rock is $\eta_{p-m} = 10^{18}$ Pa s.
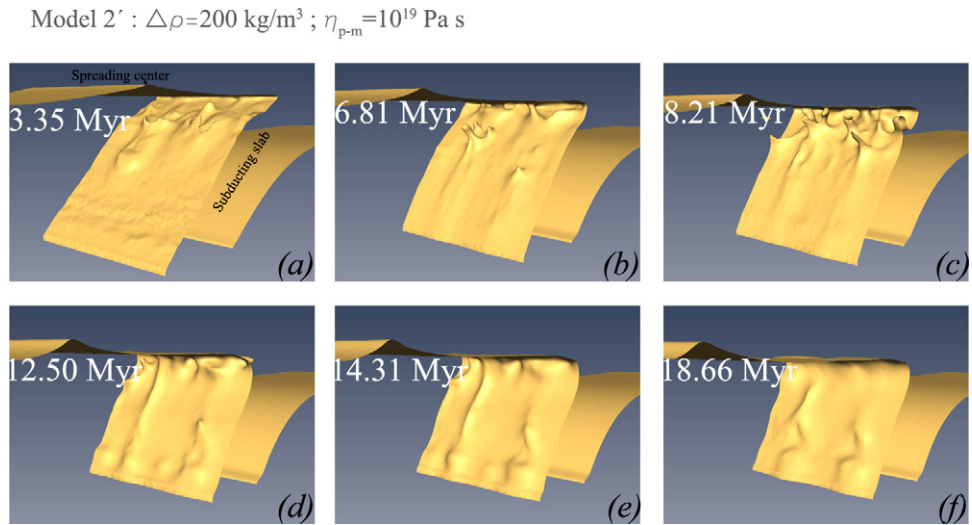

Fig. 3. Development of plumes shown by the 1350 K isosurface in models with an increased viscosity of partially molten rock ($\eta_{p-m} = 10^{19}$ Pa s), and $\triangle\rho = 200$ kg/m^3 (a–f), see model 2′ in Table 1.

close to the trench, but they tend to propagate along the slab, not directly away from the subducting slab. Gradually, another episode (6–13 Myr) occurs from the middle of the slab in a zig-zag pattern (cf. Fig. 4(a–c)), and finger/sheet-like plumes form as a front. In the later stage (13–26 Myr), big wave-like plumes appear (Fig. 4d) and are followed by the trench-normal ridges (Fig. 4(e and f)). These ridges then grow strongly. The dynamic process is generally similar to the case without any density contrast limita-
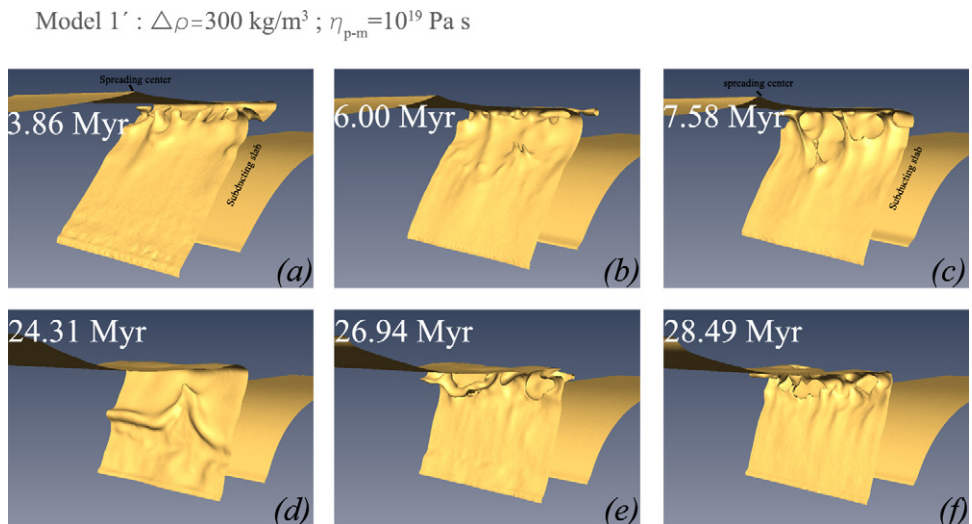

Fig. 4. Development of plumes shown by the 1350 K isosurface in the models with an increased viscosity of partially molten rock ($\eta_{p-m} = 10^{19}$ Pa s), and $\triangle\rho = 300$ kg/m^3 (a1–f1), see model 1′ in Table 1.
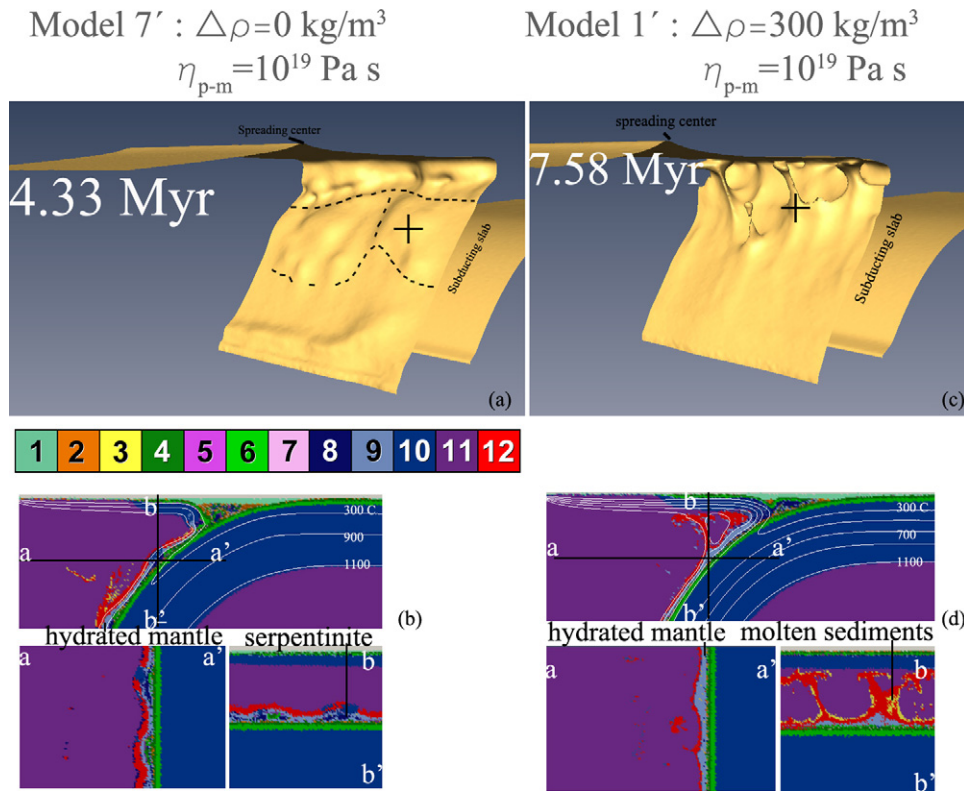
Fig. 5. (a) Dome-like instability shown by the 1350 K isosurface (model 7′ in Table 1) with an increased viscosity of partially molten rock ($\eta_{p-m} = 10^{19}$ Pa s) and $\Delta\rho = 0$ kg/m³. Dashed lines show the dome-like pattern above the slab. (b) Cross sections for the composition fields are located at a depth of 83 km shown with a plus (+) sign in Fig. 5(a). Cross section perpendicular to the trench (x-z plane) is shown in the upper panel with marks for the other two orthogonal cross-sections, and white lines show the temperature isolines on the profile. a-a′ is the horizontal cross-section (x-y plane), b-b′ is the vertical cross-section along the trench (y-z plane). (c) Finger-like plume shown by the 1350 K isosurface (model 1′ in Table 1). (d) Cross sections (at the depth of 88 km) for the compositional field of finger-like plumes in a zig-zag pattern marked with plus (+) in Fig. 5(c). Cross section perpendicular to the trench (x-z plane) is shown in the upper panel with marks for the other two orthogonal cross-sections, and white lines show the temperature isolines on the profile. a-a′ is the horizontal cross-section (x-y planes), b-b′ is the vertical cross-section along the trench (y-z plane). The color legends for the composition field are as follows: 1 = sea water; 2, 3 = sediments (2 = solid, 3 = molten), 4, 5 = basaltic crust (4 = solid, 5 = molten); 6, 7 = gabbroic crust (6 = solid, 7 = molten); 8 = serpentinized mantle, 9 = solid hydrated mantle, 10 = dry lithospheric mantle; 11 = dry asthenospheric mantle; 12 = partially molten hydrated mantle.

tion (Zhu et al., 2009), but is notably less vigorous. This implies that rapid melt removal from partially molten rock will indeed influence the wedge flow dynamics. Comparing Fig. 3(a–f) and Fig. 4(a–f), we can conclude that a higher density contrast between reference non-molten (ρ_{n-m}) and partially molten rock (ρ_{p-m}) favors the development of more vigorous cold plumes atop the slab.

3.2. Variation in lithology distribution in the mantle wedge

Here we examine the case with zero density contrast between reference non-molten (ρ_{n-m}) and partially molten rock (ρ_{p-m}), which implies instantaneous and complete melt removal (e.g. Hebert et al., 2009) (model 7′ in Table 1), with an effective partially molten rock viscosity (η_{p-m}) of 10^{19} Pa s. Randomly distributed wide dome-like instabilities develop atop the slab in a roll-like structure parallel to the trench and partly in a trench-normal way, then they separate into two parts (see Fig. 5(a)), and finally the dome-like instabilities disappear quickly. It is noteworthy that there are still instabilities (domes) atop the subducting slab for the cases without any density contrast between reference non-molten (ρ_{n-m}) and partially molten rock (ρ_{p-m}). These instabilities are formed due to the chemical buoyancy of relatively cold hydrated non-molten rock subducted atop the slab (serpentinites, oceanic crust, sediments, Fig. 5(b)) which may induce complex slab topography even in the case of complete melt removal. The composition field atop the slab indicates the details. Cross-sections (lateral section shown in the upper panel of Fig. 5(b), a-a′ section and b-b′ section are other orthogonal sections) of the composition field are located at the depth of 83 km (the coordinate of the point is (3,154,783 km), indicated with plus (+) symbol in Fig. 5(a), which show the compositional field corresponding to the development of a dome-like instability. Neutrally buoyant (according to prescribed $\Delta\rho = 0$ kg/m³) partially molten rock is the main components for the outer shell of these domes, but hydrated/serpentinized mantle, oceanic crust and sediments appear in the inner core of the domes, providing a notable source of positive buoyancy responsible for the domal growth. We also notice that the partially molten peridotite layer becomes thinner with the cooling of the overriding plate and material movement along the slab due to bending of the subducting slab.

In comparison to model 7′ with $\Delta\rho = 0$ kg/m³, models with a higher prescribed density contrast cutoff have distinctly different lithological structure above the slab, which is dominated by finger-like plumes (Model 1′, $\Delta\rho = 300$ kg/m³, Fig. 5c and d). In contrast to the dome-like structures (Fig. 5b) these plumes penetrate deep into the hot asthenospheric wedge and contain partially molten sedimentary rock intermixed with hydrated partially molten peridotite (Fig. 5d). As follows from high pressure melting experiments, such lithologically mixed plumes can produce silicic melts of trondhjemite and granodiorite compositions (Castro and Gerya, 2008).
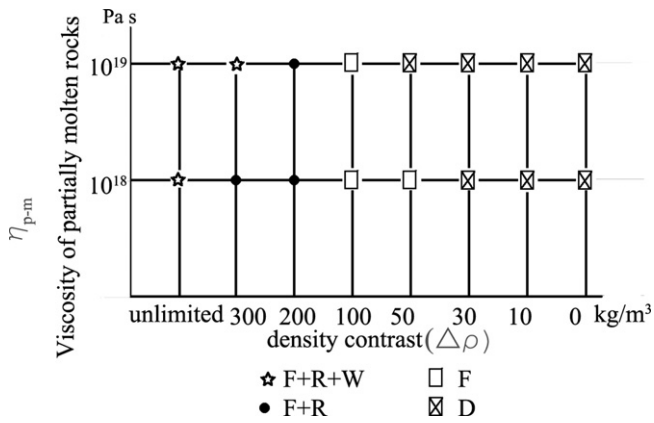
Fig. 6. Area diagram showing stability of different types of thermal–chemical structure developed atop the subducting slab as a function of density contrast cutoff ($\Delta\rho$) and effective viscosity of partially molten rock. F: Finger-like plumes; R: Trench-normal ridges; W: Wave-like plumes; and D: Dome-like instabilities and without pronounced temperature anomalies. For the case of unlimited density contrast, we used data from Zhu et al. (2009).

4. Discussion

4.1. Influence of partially molten rock buoyancy on the thermal–chemical plume patterns

In our previous work (Zhu et al., 2009), we found that the viscosity of the partially molten rock is the main controlling factor on the geometry and wavelength of thermal–chemical plumes in the mantle wedge. In particular, the lowered viscosity (10^{18}–10^{19} Pa s) of partially molten rock promotes aligned finger-like plumes originating from flattened and moderately inclined slabs, which indicates that slab dip indeed influences plume patterns (Cagnioncle et al., 2007; Grove et al., 2009). Here we additionally investigated the influence of partially molten rock buoyancy on plume morphologies. The 2-D domain diagram in Fig. 6 shows the influence of these two parameters (the effective viscosity of partially molten rock and the density contrast $\Delta\rho$ between reference non-molten (ρ_{n-m}) and partially molten rock (ρ_{p-m})) on the geometry and patterns of the plumes. By analyzing this diagram, the following important points can be made. Given a moderate limitation on the density contrast ($\Delta\rho = 300$–200 kg/m^3) between reference non-molten (ρ_{n-m}) and partially molten rock (ρ_{p-m}), it is more difficult to develop wave-like plumes atop the slab in the models with lower viscosity (10^{18} Pa s) of partially molten rock. Finger-like plumes develop in all of our models that have a density contrast cutoff $\Delta\rho$ larger than 50 kg/m^3. The three patterns of plumes (finger-like, ridge-like and wave-like) shown in our previous work (Zhu et al., 2009) can also occur for cases with density contrast larger than 200 kg/m^3 and partially molten rock viscosity of 10^{19} Pa s.

Plumes in cases with higher effective viscosities of partially molten rock develop slowly after subduction initiation and have a larger spacing between them. However, these plumes are larger since they start out later and accumulate larger volumes of hydrated partially molten rock.

4.2. Influence of partially molten rock buoyancy on the melt productivity patterns

Melt productivity above slabs directly influences volcanism. The magmatic productivity dynamics was systematically investigated in 2-D for Pacific-type convergent margins (Gorczyk et al., 2007) and retreating intraoceanic subductions (Nikolaeva et al., 2008) and the first 3-D results were reported in our previous paper (Zhu et al., 2009). Here we focus on the difference in

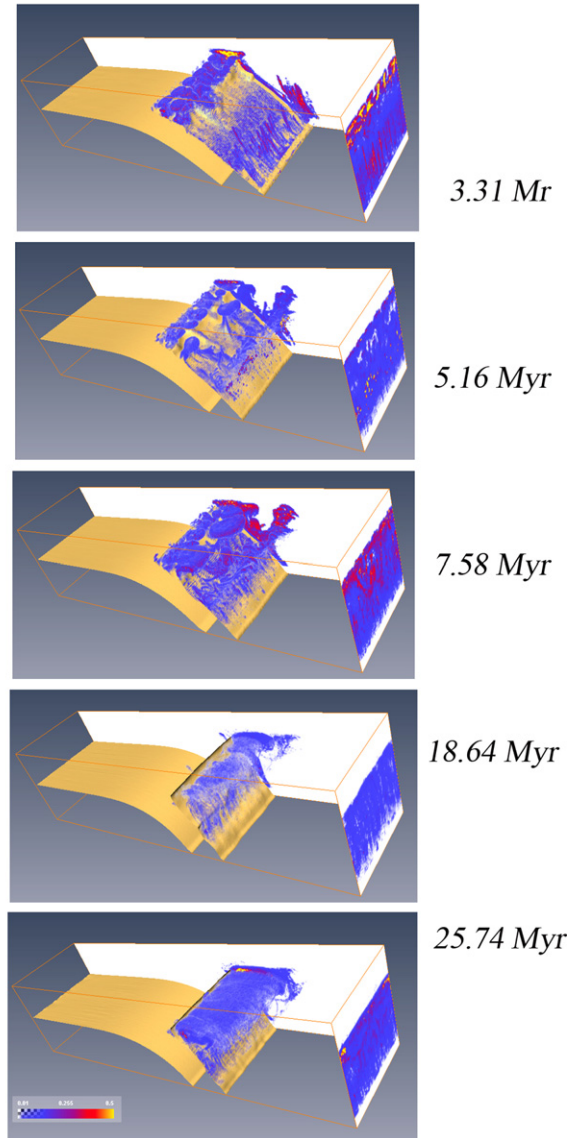Model 1′: $\triangle\rho = 300$ kg/m^3 ; $\eta_{p-m} = 10^{19}$ Pa s

Fig. 7. Evolution (at 3.31, 5.16, 7.58, 18.64 and 25.74 Myr) of volumetric melt production rate (1/Ma) shown inside the model and two projection planes with colormap for model 1′ with $\Delta\rho = 300$ kg/m^3, $\eta_{p-m} = 10^{19}$ Pa s Golden yellow shows the 1250 K temperature isosurface, which represents slab.

time-dependent melt productivity between two 3-D models with moderate ($\Delta\rho = 300$ kg/m^3) and zero ($\Delta\rho = 0$ kg/m^3) density contrast between reference non-molten (ρ_{n-m}) and partially molten rock (ρ_{p-m}) (cf. model 1′ and 7′). The calculation method for melt production is the same as described in Zhu et al. (2009) (see also Appendix): we compute melt production in situ (i.e. at depth), which is generally more than the actual amount of melt transported to the surface since part of the produced melt will remain in rock.

In Fig. 7 we show the evolution of volumetric melt production rate (1/Ma) for model 1′ with a density contrast cutoff of 300 kg/m^3. The 1250 K temperature isosurface is shown in golden yellow to delineate the slab, and volumetric melt production rate above the slab is shown inside the model and two projection planes with a colormap. These results show that the volumetric melt production rate changes spatially and episodically atop the slab. The highest volumetric melt production rates appear in the cores of the cold plumes as a result of both decompression and heating of the par-

Model 7′ : $\triangle\rho$ = 0 kg/m³; $\eta_{p\text{-}m}$ = 10¹⁹ Pa s
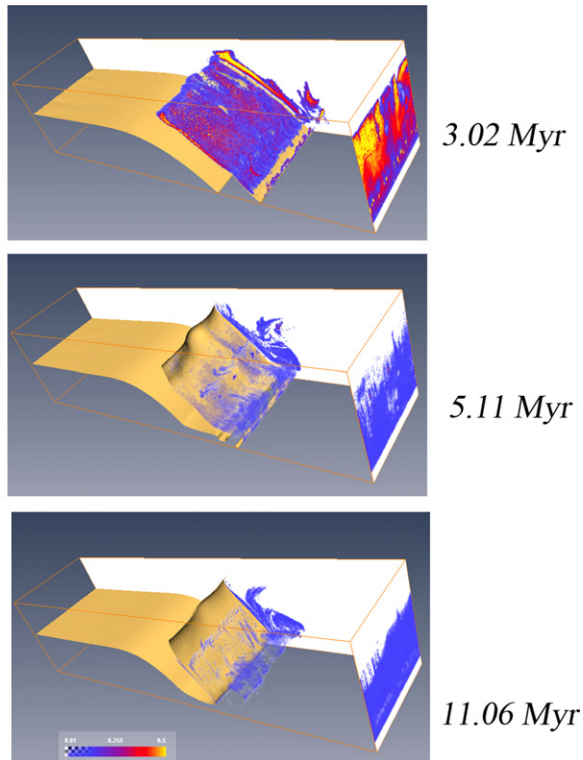

3.02 Myr

5.11 Myr

11.06 Myr

Fig. 8. Evolution (at 3.02, 5.11, 11.06 Myr) of volumetric melt production rate (1/Ma) shown inside the model and two projection planes with colormap for model 7′ with $\Delta\rho$ = 0 kg/m³, $\eta_{p\text{-}m}$ = 10¹⁹ Pa s Golden yellow shows the 1250 K temperature isosurface, which represents slab.

tially molten hydrated rock composing the plumes. The intensity of melt production is maximal after the initiation of subduction and then decreases with time because of the cooling of the overlying mantle wedge above the spontaneously retreating slab.

In Fig. 8 we show the evolution of volumetric melt production rate for model 7′ with a density contrast cutoff of 0 kg/m³. Similar to the model with moderate density contrast (Fig. 7), a higher volumetric melt production rate appears at the beginning of subduction, and then decays rapidly. Also, the distribution of melt production intensity atop the slab is strongly heterogeneous and is maximal in the cores of domal and ridge-like structures formed atop the slab. Indeed, the overall intensity of melt production in the model with $\Delta\rho$ = 0 kg/m³ is notably lower (cf. Figs. 7 and 8) than in the model with $\Delta\rho$ = 300 kg/m³, where pronounced plume structures are formed.

In Fig. 9 we show the melt productivity variation in space and time by visualizing an isosurface of melt production intensity in x-y-time space (at each moment of time, vertically integrated melt production was projected to the upper model surface to produce a series of x-y melt productivity maps). For model 1′ with a density contrast cutoff of 300 kg/m³ between non-molten (ρ_{n-m}) and partially molten rock (ρ_{p-m}), melt productivity is relatively high. In Fig. 9(a and b) the isosurface of 0.23 km³/km²/Myr (km/Myr) shows, in two different viewpoints, the evolution of melt productivity for this model in both space and time. In Fig. 9(e) we have also shown variations in the spatial intensity of the melt production beneath the surface for model 1′. During the first 6 Myrs of the numerical simulation, high magmatic productivity is distributed in a large area, then it decays to almost zero, then later it grows again. The trench-parallel two line structure (with 50–150 km trench-orthogonal spacing) varies with time. For model 7′ with zero

density contrast between non-molten (ρ_{n-m}) and partially molten rock (ρ_{p-m}), the overall melt productivity is high within the first 4 million years after subduction initiation (Fig. 9f; 3.02–3.59 Myr) but then it decreases notably compared to model 1′ (cf. Fig. 9e and f). In both models, initially high magmatic productivity is distributed in a relatively large area, and then focuses into a trench-parallel line of magmatic maxima keeping a spatially variable small-scale pattern corresponding to the activity of individual dome-like and finger-like structures. It is also noteworthy that a high intensity of melt production was indeed suggested for the initial stages of spontaneous subduction initiation based on geological data (e.g. Stern, 2004) that is consistent with our models (Figs. 7–9).

We conclude that the density contrast ($\Delta\rho$) between non-molten (ρ_{n-m}) and partially molten rock (ρ_{p-m}) notably affects the magnitude of melt productivity: it is higher in models with larger density contrast ($\Delta\rho$). On the other hand, the following gross-scale melt productivity pattern is characteristic for all models: there is a higher magmatic productivity in a wide area above the steepening slab during 5–10 Myr after subduction initiation, this productivity decays later on, then grows again episodically in a much narrower area. Trench-parallel two line structures (with 50–150 km trench-orthogonal spacing) chaining contemporaneous melt productivity centers appear episodically in time. Inherent clustering and periodicity of melt production in our thermal–chemical models is mainly related to the growth dynamics of individual thermal–chemical plumes and domal structures atop the slab. Thermal–chemical plumes and related melt production in the presented models occur episodically (Figs. 4f and 7; Model 1′) during a long time through the entire model development (up to >30 Myr from subduction initiation). Therefore, our model could possibly explain volcanism in both young and mature subduction systems. For example, modeled periodicity and spatial clustering of melt production correlate well with periodicity and spatial clustering of volcanism in North East Japan inferred from the chronological and stratigraphic studies (e.g. Honda and Yoshida, 2005; Zhu et al., 2009).

It is also important to mention that the melt productivity pattern characteristic of the beginning of our experiments (i.e. for the first 5–10 Myr) is strongly affected by the subduction initiation process (e.g. Stern, 2004) associated with changes in the slab dip angle and significant cooling of the overriding plate. Changes in the melt productivity distribution and intensity from subduction initiation toward more mature stages are shown in Fig. 9 where an initially broad (150–200 km) melt production area narrows toward the more focused (50–70 km wide) magmatic front in 5–10 Myr after the initiation of retreating subduction.

4.3. Dynamical influences of H_2O migration velocity

The addition of water results in a reduction of the melting temperature of the surrounding mantle, and subsequently lowers its density and viscosity due to the melt presence. Thus, the H_2O migration velocity from the slab is one of the key parameters to impact the distribution and amount of partially molten rock in the mantle wedge. In our models discussed above, we have taken a constant H_2O migration velocity of 10 cm/year. Indeed, the actual velocity can be greatly variable in nature depending on the mantle permeability and the viscosity of the aqueous fluid (e.g. Iwamori, 1998; Cagnioncle et al., 2007). The degree of melting increases with water content in the H_2O-undersaturated conditions at the same P-T conditions (Hirose and Kawamoto, 1995). Smaller H_2O migration velocity may thus decrease the extent of the hydrous (i.e. fluid fluxed) melting in the mantle wedge. To test this effect, we have run additional simulations with smaller H_2O migration velocity (1 cm/year and 0.1 cm/year) for the model with no cutoff value for the density contrast between non-molten (ρ_{n-m}) and partially molten rock (ρ_{p-m}). The effective viscosity of partially molten rock
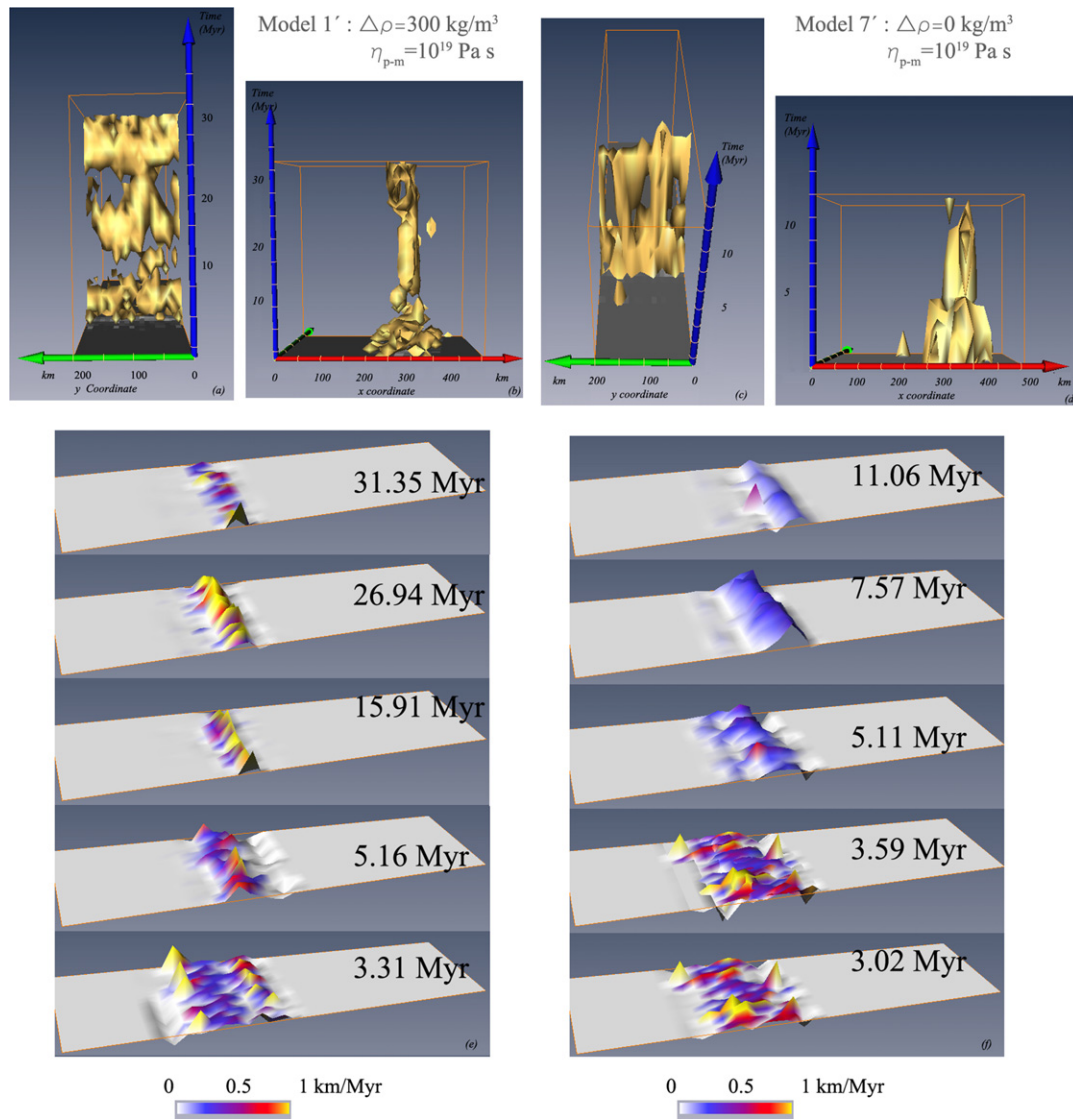
Fig. 9. Spatial and temporal evolution of the intensity of melt production shown by isosurfaces of melt production beneath the surface of the model. The numerals for time indicate the time since the beginning of the experiments. (a and b) and (c and d): Isosurfaces from two different viewpoints of melt productivity at 0.23 km^3/km^2/Myr for model 1′ and 7′; (e) and (f):Variation in the spatial intensity of melt production beneath the surface (in *x-y* plane) of the model 1′ and 7′ with time since the beginning of experiment. Note that the time scales for Model 1′ and Model 7′ are different.

in these runs was $\eta_{p-m} = 10^{18}$ Pa s. During the first 30 Myr from the start of calculation and for the case with lowered (1 cm/year) H_2O migration velocity, there are mushroom-like plumes and wave-like plumes in a zig-zag pattern, but there are no obvious ridge-like plumes except at the beginning of the subduction. Furthermore, for the case with the lowest (0.1 cm/year) H_2O migration velocity, there is only a weak tendency to develop Rayleigh-Taylor instabilities. Indeed, in this case there is not enough melt-related positive buoyancy atop the slab to develop pronounced thermal–chemical plumes propagating away from the slab and only low-amplitude domal structures are formed. This result is very similar to the cases with high (10 cm/year) H_2O migration velocity where melt-related positive buoyancy atop the slab was reduced by prescribing a low ($\Delta\rho = 0$–50 kg/m^3) cutoff value for the density contrast between non-molten and partially molten rock (Fig. 2d–f). In both cases, partially molten rock is mainly distributed atop the slab with a thinner partially molten layer (Fig. 5b). Also, in experiments with lowered H_2O migration velocity, a thinner rheologically weak hydrated layer is formed atop the slab. Therefore, plates are more coupled and the retreating trench velocity is notably reduced, which is con-

sistent with 2-D results on plate coupling and decoupling processes (Gorczyk et al., 2007).

5. Conclusions

In this study, we investigate how the buoyancy of partially molten rock affects the development of thermal–chemical plumes and melt productivity in the mantle wedge in 3-D by using a simplified cutoff approach for the density contrast ($\Delta\rho$) between non-molten (ρ_{n-m}) and partially molten rock (ρ_{p-m}). We find that the three patterns of thermal–chemical plumes (finger-like, ridge-like and wave-like) found in our previous paper (Zhu et al., 2009) are only stable in experiments with $\Delta\rho > 200$ kg/m^3 (i.e. low to moderate degree of melt removal). Finger-like plumes develop for a broader range of density contrast cutoff values ($\Delta\rho > 50$ kg/m^3, implying moderate to high degree of melt removal). Strongly lowered density contrast cutoffs (0–50 kg/m^3, implying high to complete melt removal) suppress pronounced plumes and are associated with low-amplitude (50–100 km wide and 10–15 km high) domal structures developing atop the slab due to the chemical

buoyancy of subducted hydrated non-molten rock types (oceanic crust, sediments and serpentinites).

Magmatic productivity below the surface varies in both space and time: clustering of the melt productivity in space (with 20–100 km lateral spacing) and time (with 1–6 Myr periodicity) is observed in all models. The density contrast ($\Delta\rho$) between non-molten (ρ_{n-m}) and partially molten rock (ρ_{p-m}) mainly affects the magnitude of melt productivity: overall productivity is notably higher for cases with pronounced hydrated thermal–chemical plumes developed in the mantle wedge. Melt productivity clustering is mainly related to the activity of individual thermal–chemical structures growing atop slabs (plumes, domes). This clustering may explain spatial and temporal variations of magmatic activity and crustal growth in intraoceanic arcs, such as spatial–temporal periodicity of the quaternary volcano distribution in North-East Japan (Honda and Yoshida, 2005; Kimura and Yoshida, 2006), the average spacing between volcanic centers along Kermadec arc (de Ronde et al., 2007), and the spatial periodicity of crustal thickness variations along the Izu intra-oceanic arc (e.g. Kodaira et al., 2006).

Acknowledgements

Appendix A. Supplementary data

Supplementary data associated with this article can be found, in the online version, at doi:10.1016/j.pepi.2011.02.005.

References

Arcay, D., Tric, E., Doin, M.P., 2005. Numerical simulations of subduction zones: effect of slab dehydration on the mantle wedge dynamics. Phys. Earth Planet. Inter. 149, 133–153.

Asimow, P.D., Langmuir, C.H., 2003. The importance of water to oceanic mantle melting regimes. Nature 421, 815–819, doi:10.1038/nature01429.

Cagnioncle, A.M., Parmentier, E.M., Elkins-Tanton, L.T., 2007. Effect of solid flow above a subducting slab on water distribution and melting at convergent plate boundaries. J. Geophys. Res. 112, B09402, doi:10.1029/2007JB004934.

Castro, A., Gerya, T.V., 2008. Magmatic implications of mantle wedge plumes: experimental study. Lithos 103, 138–148, doi:10.1016/j.litjos.2007.09.012.

Connolly, J.A.D., Petrini, K., 2002. An automated strategy for calculation of phase diagram sections and retrieval of rock properties as a function of physical conditions. J. Metamorph. Geol. 20, 697–708.

Connolly, J.A.D., Schmidt, M.W., Solferino, G., Bagdassarov, N., 2009. Permeability of asthenospheric mantle and melt extraction rates at mid-ocean ridges. Nature 462, 209–214, doi:10.1038/nature08517.

Davies, J.H., Stevenson, D.J., 1992. Physical model of source region of subduction zone volcanics. J. Geophys. Res. 97 (B2), 2037–2070.

de Ronde, C.E.J., et al., 2007. Submarine hydrothermal activity along the mid-kermadec Arc, New Zealand: large-scale effects on venting. Geochem. Geophys. Geosyst. 8 (Q07007), doi:10.1029/2006GC001495.

Faccenda, M., Gerya, T.V., Chakraborty, S., 2008. Styles of post-subduction collisional orogeny: influence of convergence velocity, crustal rheology and radiogenic heat production. Lithos 103, 257–287.

Gerya, T.V., Yuen, D.A., 2003a. Characteristics-based marker-in-cell method with conservative finite-differences schemes for modeling geological flows with strongly variable transport properties. Phys. Earth Planet. Inter. 140, 293–318.

Gerya, T.V., Yuen, D.A., 2003b. Rayleigh-Taylor instabilities from hydration and melting propel 'cold plume's at subduction zones. Earth Planet. Sci. Lett. 212, 47–62.

Gerya, T.V., Yuen, D.A., Sevre, E.O.D., 2004c. Dynamical causes for incipient magma chambers above slabs. Geology 32, 89–92.

Gerya, T.V., Yuen, D.A., 2007. Robust characteristics method for modelling multiphase visco-elasto-plastic thermo-mechanical problems. Phys. Earth Planet. Inter. 163, 83–105.

Gerya, T.V., Connolly, J.A.D., Yuen, D.A., Gorczyk, W., Capel, A.M., 2006. Seismic implications of mantle wedge plumes. Phys. Earth Planet. Inter. 156, 59–74.

Gerya, T.V., 2010. Introduction to numerical geodynamic modelling. Cambridge University Press (Chapter 14 and 15).

Gorczyk, W., Gerya, T.V., Connolly, J.A.D., Yuen, D.A., Rudolph, M., 2006. Large-scale rigid-body rotation in the mantle wedge and its implications for seismic tomography Geochem. Geophys. Geosyst. 7, doi:10.1029/2005GC001075.

Gorczyk, W., Willner, A.P., Gerya, T.V., Connolly, J.A.D., Burg, J.P., 2007. Physical controls of magmatic productivity at Pacific-type convergent margins: Numerical modelling. Phys. Earth Planet. Inter. 163, 209–232.

Grove, T.L., Chatterjee, N., Parman, S.W., Medard, E., 2006. The influence of H_2O on mantle wedge melting. Earth Planet. Sci. Lett. 249, 74–89.

Grove, T.L., Till, C.B., Lev, E., Chatterjee, N., Medard, E., 2009. Kinematic variables and water transport control the formation and location of arc volcanoes. Nature 459, 694–697, doi:10.1038/nature08044.

Hawkesworth, C.J., Turner, S.P., McDermott, F., Peate, D.W., van Calsteren, P., 1997. U-Th isotopes in arc magmas: implications for element transfer from the subducted crust. Science (USA) 276, 551–555.

Hebert, L.B., Antoshechkina, P., Asimow, P., Gurnis, M., 2009. Emergence of a low-viscosity channel in subduction zones through the coupling of mantle flow and thermodynamics. Earth Planet. Sci. Lett. 278, 243–256.

Hirose, K., Kawamoto, T., 1995. Hydrous partial melting of lherzolite at 1 GPa: The effect of H_2O on the genesis of basaltic magmas. Earth Planet. Sci. Lett. 133, 463–473.

Honda, S., Saito, M., Nakakuki, T., 2002. Possible existence of small-scale convection under the back arc. Geophys. Res. Lett. 29, 2043, doi:2010.1029/2002GL015853.

Honda, S., Yoshida, T., 2005. Application of the model of small-scale convection under the island arc to the NE Honshu subduction zone. Geochem. Geophys. Geosyst. 6, Q01002, doi:10.1029/2004GC000785.

Honda, S., Gerya, T.V., Zhu, G., 2010. A simple model of thermal–chemical convection in the mantle wedge. Earth Planet. Sci. Lett. 290, 311–318.

Iwamori, H., 1998. Transportation of H_2O and melting in subduction zones. Earth Planet. Sci. Lett. 160, 65–80.

Karato, S., Wu, P., 1993. Rheology of the upper mantle: a synthesis. Science 260, 771–778.

Kimura, J., Yoshida, T., 2006. Contributions of slab fluid, mantle wedge and crust to the origin of quaternary lavas in the NE Japan arc. J. Petrol. 47, 2185–2232, doi:10.1093/petrology/egl041.

Kodaira, S., Sato, T., Takahashi, N., Ito, A., Tamura, Y., Tatsumi, Y., Kaneda, Y., 2006. Seismological evidence for variable growth of crust along the Izu intraoceanic arc. J. Geophys. Res. 112, Article Number: B05104.

Mysen, B.O., Boettcher, A.L., 1975. Melting of a hydrous mantle: II. Geochemistry of crystals and liquids formed by anatexis of mantle peridotite at high pressures and high temperatures as a function of controlled activities of water, hydrogen, and carbon dioxide. J. Petrol. 16, 549–593.

Nikolaeva, K., Gerya, T.V., Connolly, J.A. D., 2008. Numerical modelling of crustal growth in intraoceanic volcanic arcs. Phys. Earth Planet. Inter., doi:10.1016/j.pepi.2008.1006.1026.

Peacock, S.M., 1990. Fluid processes in subduction zones. Science 248, 329–337.

Plank, T., Cooper, L.B., Manning, C.E., 2009. Emerging geothermometers for estimating slab surface temperatures. Nat. Geosci. 2, 611–615.

Poli, S., Schmidt, M.W., 1995. H_2O transport and release in subduction zones: experimental constraints on basaltic and andesitic systems. J. Geophys. Res. 100, 22298–22314.

Schmidt, M.W., Poli, S., 1998. Experimentally based water budgets for dehydrating slabs and consequences for arc magma generation. Earth Planet. Sci. Lett. 163, 361–379.

Stern, R.J., 2002. Subduction zones. Rev. Geophys., 40, 1012, doi:1010.1029/2001RG000108.

Stern, R.J., 2004. Subduction initiation: spontaneous and induced. Earth Planet. Sci. Lett. 226, 275–292.

Tamura, Y., Tatsumi, Y., Zhao, D.P., Kido, Y., Shukuno, H., 2002. Hot fingers in the mantle wedge: new insights into magma genesis in subduction zones. Earth Planet. Sci. Lett. 197, 105–116, doi:10.1016/S0012-821X(02)00465-X.

van Keken, P.E., Kiefer, B., Peacock, S.M., 2002. High-resolution models of subduction zones: implications for mineral dehydration reactions and the transport of water into the deep mantle. Geochem. Geophys. Geosyst. 3 (10), 1056, doi:10.1029/2001GC000256.

Zhao, D., Mishra, O.P., Sanda, R., 2002. Influence of fluids and magma on earthquakes: seismological evidence. Phys. Earth Planet. Inter. 132, 249–267.

Zhao, D., 2009. Multiscale seismic tomography and mantle dynamics. Gondwana Res. 15, 297–323.

Zhu, G., Gerya, T.V., Yuen, D., Honda, S., Yoshida, T., Connolly, J.A.D., 2009. Three-dimensional dynamics of hydrous thermal–chemical plumes in oceanic subduction zones. Geochem. Geophys. Geosyst. 10 (Q11006), doi:10.1029/2009GC002625.